Elastic properties of amorphous TiNiSn

Music, Denis; Hajas, Balint ; Mayrhofer, Paul ; Khayyamifar, Sana ; Sadowski, Grzegorz ; Hektor, Johan; Olsson, Pär

Published in:
Journal of Physics: Condensed Matter

DOI:
10.1088/1361-648X/ae3c75

2026

Document Version:
Publisher's PDF, also known as Version of record

Elastic properties of amorphous TiNiSn

Journal of Physics: Condensed Matter

PAPER

Elastic properties of amorphous TiNiSn

Denis Music[1,2,*], **Balint I Hajas**[3], **Paul H Mayrhofer**[3], **Sana Khayyamifar**[1,2], **Grzegorz Sadowski**[1,2], **Johan Hektor**[1,2] and **Pär A T Olsson**[1,4]

[1] Department of Materials Science and Applied Mathematics, Malmö University, SE-205 06 Malmö, Sweden
[2] Biofilms Research Centre for Biointerfaces, Malmö University, SE-205 06 Malmö, Sweden
[3] Institute of Materials Science and Technology, Getreidemarkt 9, TU Wien, A-1060 Vienna, Austria
[4] Division of Mechanics, Materials and Component Design, Lund University, PO Box 118, SE-221 00 Lund, Sweden
[*] Author to whom any correspondence should be addressed.

E-mail: denis.music@mau.se

OPEN ACCESS

RECEIVED
31 October 2025

REVISED
18 December 2025

ACCEPTED FOR PUBLICATION
22 January 2026

PUBLISHED
4 February 2026

Keywords: amorphous, TiNiSn, elasticity, density functional theory, machine learning

Supplementary material for this article is available online

Abstract

The elastic properties of amorphous TiNiSn, a promising half-Heusler system for flexible and wearable devices, were investigated using experimental and theoretical methods. Nanoindentation measurements performed on amorphous TiNiSn thin film grown by magnetron sputtering yielded an elastic (Young's) modulus value of 132 GPa. To corroborate this result, density functional theory (DFT) calculations and two machine learning models were employed, where the latter were trained on available literature data. The DFT-derived elastic modulus of amorphous TiNiSn is 113 GPa (stress-free conditions), which is 15% lower than the experimental value. However, when hydrostatic stress is considered, arising from possible thermal loads and ion bombardment during thin film synthesis, the difference is reduced to 5%. Electronic structure analysis reveals that amorphous TiNiSn exhibits predominantly covalent bonding with a minor metallic contribution, which is consistent with the measured elastic modulus. Although both machine learning models underestimate the experimental modulus more than DFT, the theoretical results enhance understanding of the elastic behaviour of amorphous TiNiSn and highlight its potential for future applications in flexible microelectronic systems.

1. Introduction

Heusler alloys constitute a class of intermetallic compounds composed of transition metals (X, Y) and a main-group element (Z) [1–4]. These alloys encompass an extensive range of interesting physical properties including magnetism, semiconducting behaviour, half-metallicity and good thermoelectric response [1, 2, 5–7]. These solids can be classified into full-Heusler alloys with the formula X_2YZ (50.0 at.% X, 25.0 at.% Y, 25.0 at.% Z, space group Fm-3 m) [1] and half-Heusler alloys with the formula XYZ (33.3 at.% X, 33.3 at.% Y, 33.3 at.% Z, space group F-43 m) [8]. For instance, Co_2MnGa is a full-Heulser alloy and TiNiSn is a half-Heusler compound [1–4]. Full-Heusler alloys often exhibit metallic or half-metallic electronic structures and ferromagnetism [9, 10]. Due to one metallic spin channel and one semiconducting, full-Heusler alloys are promising for spintronic applications, magnetic tunnel junctions and sensors, to name a few [9, 10]. Half-Heusler alloys possess intrinsic vacancies, which leads to semiconducting or narrow-gap electronic behaviour [2, 11]. They have attracted extensive attention for thermoelectric applications, as their electrical conductivity and Seebeck coefficient can be adjusted through doping [12, 13]. Their lower lattice thermal conductivity, compared to full-Heusler alloys, arises from phonon scattering due to local structural disorder [12]. Nonetheless, their mechanical brittleness still poses a challenge [1, 14].

Amorphous solids lack long-range ordering, which leads to unique physical properties [15, 16]. Among them, amorphous Heusler alloys have attracted considerable attention due to their unusual electronic, thermal and magnetic properties. In amorphous systems, additional scattering mechanisms for

charge carriers and phonons become active, enabling the tuning of thermal conductivity, a strategy that has already been demonstrated for half-Heusler alloys [17]. Notably, amorphous Ni–Mn–In Heusler alloy exhibits higher magnetisation at elevated temperatures than the corresponding crystalline counterpart [18]. Similarly, Co_2MnGa retains ferromagnetic behaviour in its amorphous state [19]. Amorphous half-Heusler TiNiSn is superconductive [20] and seems to be flexible [21]. The latter property is particularly relevant for wearable microelectronic devices (e.g. self-powered biomedical sensors, stretchable superconducting interconnects, integrated devices for soft robotics, smart clothing), where mechanical characteristics play a crucial role. However, such data remain scarce and warrant further investigation.

In this work, we explore elastic properties of amorphous TiNiSn, a promising thermoelectric system for flexible electronic applications. Amorphous TiNiSn thin films are grown by magnetron sputtering, and an elastic (Young's) modulus is obtained by nanoindentation (NI). To rationalise the experimental data, density functional theory (DFT) and two machine learning models are employed. These machine learning models are based on available literature data, as described below, and features (descriptors) need to be generic to enable an estimation of the elastic modulus of amorphous TiNiSn.

2. Methods

2.1. Synthesis and characterisation

TiNiSn thin films were grown by direct current magnetron sputtering to facilitate experimental validation. A Si substrate was used without intentional heating and rotated at 20 rpm to achieve uniformity. Elemental targets of Ti (99.95% purity, power density 6.9 W cm^{-2}), Ni (99.9% purity, power density 2.0 W cm^{-2}) and Sn (99.9% purity, power density 1.2 W cm^{-2}) were placed 12.5 cm from the substrate and at a 40° inclination angle to the substrate normal. The base pressure was approximately 3×10^{-6} Pa, and the working pressure was 0.5 Pa (Ar atmosphere). The composition of the TiNiSn thin film was determined by energy dispersive x-ray analysis (EDX). Energy calibration of the EDX detector was performed using a Co reference sample and 3 measurements were carried out at an accelerating voltage of 15 kV. The following composition was obtained: 30 ± 1 at.% Ti, 35 ± 1 at.% Ni and 35 ± 1 at.% Sn (19 ± 1 wt.% Ti, 27 ± 1 wt.% Ni and 54 ± 1 wt.% Sn), henceforth referred to as TiNiSn. The structure was analysed by employing grazing incidence wide angle x-ray scattering indicating that the TiNiSn sample was amorphous. These data can be found elsewhere (equivalent sputtering conditions were applied previously) [21]. Finally, mechanical properties were determined using NI (continuous stiffness measurements) based on the method introduced by Oliver and Pharr [22]. A Berkovich diamond tip, with the tip area function calibrated on fused silica, was used in these experiments. Approx. 50 indents were made with a maximum penetration depth less than 10% of the sample thickness (forces ranged from 10 to 200 mN). Poisson's ratio of 0.314 was used, as determined via theoretical modelling in this work.

2.2. Theoretical modelling

Two theorical approaches were employed: DFT and machine learning. Since TiNiSn and ZrNiSn exhibit the same crystal structure, an amorphous TiNiSn configuration was obtained by replacing Zr with Ti in an amorphous ZrNiSn cell (324 atoms) from the previous work [23]. The original amorphous ZrNiSn cell was derived by employing a liquid-quench method [24]. After replacing Zr with Ti, the cell was thermalised and fully relaxed at 0 K, achieving consistency with the previous work (experimental neutron data) [20]. Since the crystalline counterpart is cubic, the amorphous configuration was constrained to the same symmetry. TiNiSn is paramagnetic even at low temperatures [25] and hence the DFT modelling was carried out without spin polarisation. The Vienna *ab initio* simulation package (VASP) was used in all DFT calculations. The projector-augmented plane-wave potentials [26–28] were employed in the VASP code at the Perdew, Burke and Ernzerhof [29] level of (generalised gradient) approximation. Full structural optimisation was carried out by minimising the interatomic forces in amorphous TiNiSn. The convergence criterion for the total energy was set to 0.01 meV per atom and a 500 eV cut-off was employed. The integration in the Brillouin zone was done on a Monkhorst-Pack $4 \times 4 \times 4$ k-point mesh [30]. All cubic elastic constants were calculated, as described elsewhere [31], which allowed for the estimation of the elastic modulus and Poisson's ratio [32]. The electronic structure was analysed using VESTA [33].

In an attempt to create a predictive data-driven model, a dataset containing 625 amorphous systems (see the supplementary material) was used as input for machine learning: bulk metallic glasses (BMGs) [34–39], SiO_2-based glasses [40, 41], diamond-like carbon (DLC) [42] and other amorphous materials (e.g. boron-rich solids) [23, 43–47]. No data on amorphous TiNiSn were included and predictability of

machine learning models relied on generic features. Two models were considered: artificial neural network (ANN) and gradient boosting regression (GBR). The Python code used for ANN can be found elsewhere [48], while the one for GBR is available in the supplementary material. The dataset was normalised (rescaled) to ensure consistency (coherent scale for all input data). Features were then selected: x_1 (mass density) and x_2 (average molar mass), as motivated below. These features are expected to be accessible to both theoreticians and experimentalists, proving simplicity to the model and possibly usability. The performance (accuracy) was assessed using the coefficient of determination [49].

The architecture of the ANN was created, containing the number of hidden layers and neurons per layer to maximise the accuracy [49]. Between one and three hidden layers were probed and the model with the highest accuracy was used further. The activation function [49] was the hyperbolic tangent and a regularisation strength of 10^{-4} (the Ridge estimator) was chosen to avoid overfitting. The learning rate was kept constant. The dataset was split into training and testing sets, and the ANN was first run with the training set (80% of the data) and the predictability was evaluated on the remainder. The LBFGS solver (the improved Broyden-Fletcher-Goldfarb-Shanno algorithm) was selected for optimisation [49]. The scikit-learn implementation of GBR was used within a pipeline that included polynomial feature expansion to account for feature interactions [50]. Model hyperparameters, including the number of estimators, learning rate, maximum tree depth, minimum sample splits and subsampling ratio, were optimised using a grid search with 5-fold cross-validation to minimise errors. Model performance was evaluated on a withheld 20% test subset, as in the case of ANN. Feature importance values were computed to assess the relative influence of each input variable on the model predictions.

3. Results and discussion

Since TiNiSn samples are amorphous, they appear flat and featureless on a Si substrate, as shown previously [21], so that morphology is not expected to have any influence on the characterisation of the mechanical properties. The experimental (NI) value of elastic modulus for amorphous TiNiSn is 132 $\pm$ 1 GPa. To rationalise this outcome, DFT and two machine learning models were employed. While DFT can straightforwardly provide a theoretical value, machine learning is more challenging since deriving a model for prediction of physical properties relies on a selection of features (descriptors). The space of possible features in machine learning is usually vast, and many relevant features may not be known *a priori* so that hypotheses are required. It is often attempted to identify which features logically or scientifically affect the desired outcome. Structural features often involve parameters such as coordination number and bond length [51]. Conversely, chemical features typically include elemental properties such as effective charge, atomic radius, molar mass and electronegativity [51]. A model for BMGs employing ANN has recently been proposed [52]. By incorporating molar mass, number of constituent elements, yield strength and glass transition temperature as features, the ANN model can predict the elastic modulus of BMGs [52]. However, some of these features, such as the glass transition temperature, are process-dependent, which complicates or even inhibits generalisation. For instance, there are no reports on the glass transition temperature of DLC or Heusler alloys. Furthermore, a recent machine learning model for the bulk and shear moduli of SiO_2-based glasses relied on physics-informed features, which were based on classical interatomic potentials [40]. Notably, these types of amorphous solids were characterised using entirely different sets of features, highlighting the challenge of developing a unified modelling approach. After careful assessment of possible features and critical data availability, mass density (x_1) and average molar mass (x_2) were selected in the current work.

The dataset used in the machine learning models is provided in figure 1. It appears that the elastic modulus values scale with mass density (figure 1(a)) and average molar mass (figure 1(b)), but drawing any general conclusions seems unfeasible. There are reports claiming that the elastic modulus is a linear or exponential function of mass density, as exemplified by DLC [42] and Al_2O_3 [53], but starkly different slopes appear when various systems are simultaneously considered, as seen in figure 1(a). Mass density can be perceived as a cumulative feature encapsulating a lot of physical, chemical and structural information. For instance, the atomic radius is explicitly included as larger atoms may reduce how tightly packed a solid can be. Another contribution comes from packing efficiency, as a higher packing density should lead to a higher mass density, which is also related to the type of chemical bonds (ionic, covalent, metallic) found in these solids. It can also be argued that heavier atoms increase the mass density, which is why the second machine learning feature considered here is the average molar mass (see figure 1(b)). The molar mass is related to the mass density, but the use of the mass density only is questionable, as argued above (diverse slopes for DLC [42] and Al_2O_3 [53]). All these aspects may affect the elastic properties implicitly and provide challenges for machine learning modelling in general.

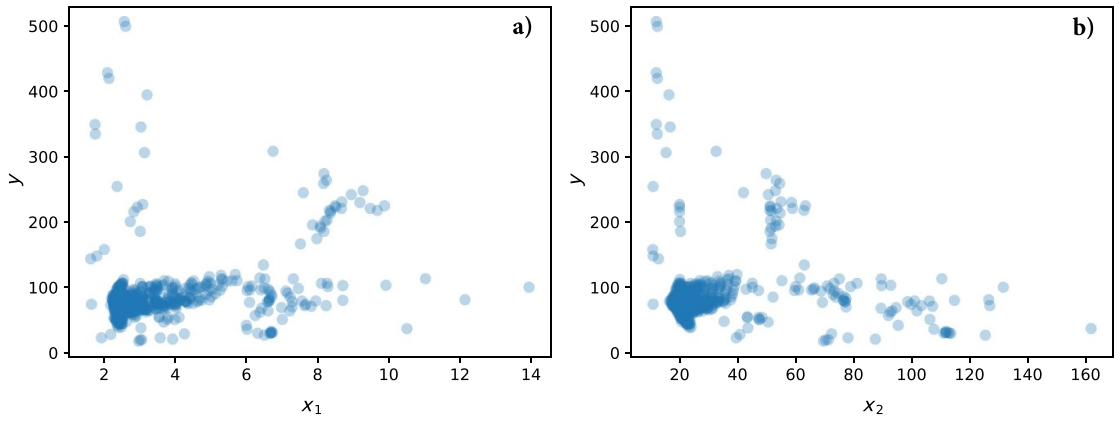

Figure 1. The machine learning dataset used in the current work. The parameter y is the elastic modulus in GPa, x_1 specifies the mass density in g cm^{-3} (a) and x_2 is the average molar mass in g mol $^{-1}$ (b).

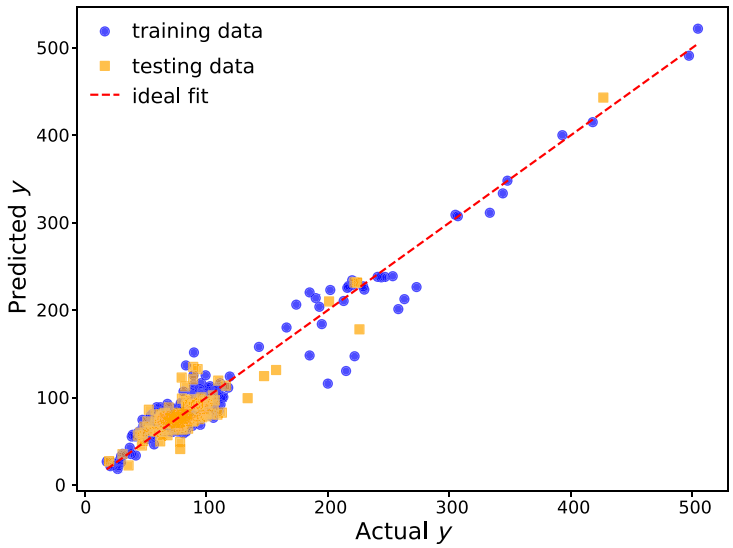

Figure 2. Artificial neural network (ANN) model with two hidden layers. The parameter y is the elastic modulus in GPa. The accuracy (score) of 89% was obtained, as evaluated by the coefficient of determination. The mean squared error was 238 (GPa)^2. The input was randomly split into training and testing datasets (random state 42 in Python to enable reproducibility).

Using an ANN model with two hidden layers, one with 200 neurons and the other with 100 neurons, 89% accuracy can be reached, as depicted in figure 2. Hence, the elastic modulus data can be described in the full range from approximately 30–500 GPa, and the selected feature space suffices to account for the whole diversity, ranging from different bonding types (predominantly ionic bonding in SiO_2-based glasses, metallic bonding in BMGs and covalent in DLC) to highly different mass densities. It is also important to state that regularisation and only two hidden layers were used, which may inhibit overfitting. It is expected that the selected features (x_1 and x_2) can easily be utilised by experimentalists (density from direct measurements, x-ray reflectivity, pair correlation functions and the like; molar mass directly from composition and the periodic table of elements) and theoreticians (density from the composition and equilibrium volume) giving rise to a broad applicability (screening for novel systems). No growth-related parameters are needed for this data-driven model.

Another machine learning model employed in this work was GBR and the outcome is provided in figure 3. Comparing the ANN and GBR models, the overall performance of the ANN model is better (89% vs. 76% accuracy, respectively), but it should be stated that the worse performance of the GBR model is likely due to two outliers (see figure 3), while most of the data are well aligned. Both models (figures 2 and 3) perform better above 250 GPa. In general, an ANN model may perform slightly better due to highly nonlinear mappings between input and output through its hidden layers and nonlinear activation functions. Since there are fewer features in the current work, each layer's parameters can be tuned effectively to capture relevant interactions. GBR models such interactions implicitly through tree

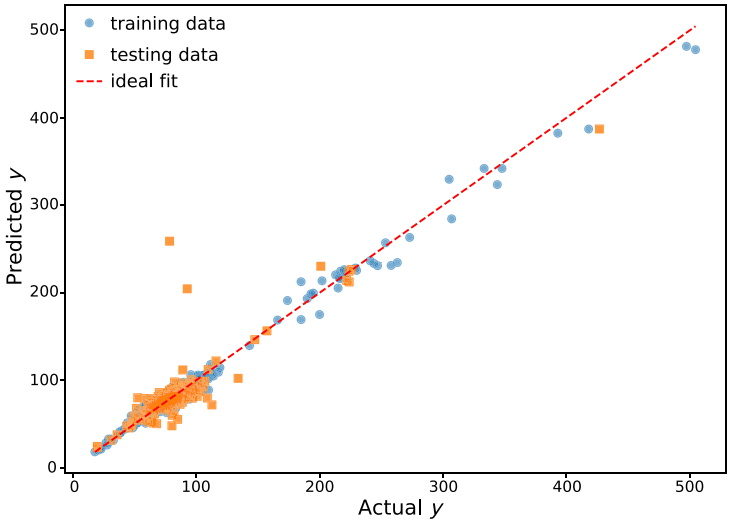

Figure 3. Gradient boosting regression (GBR) model with the same data as in the ANN model. The parameter y is the elastic modulus in GPa. The accuracy (score) of 76% was obtained, as assessed by the coefficient of determination. The mean squared error was 506 $(GPa)^2$.

splits but only in a hierarchical, discrete way, while ANNs can model them jointly and smoothly. An important issue in machine learning is the selection of features. Two features were identified in the current work, namely mass density and average molar mass, but it is conceivable that additional features may improve these two models. One such feature is the average bond length, but less than 5% of the used data would allow for such modelling, which is insufficient for both ANN and GBR. Thus, more data collection is required in future efforts. It remains to be seen how both machine learning models perform for amorphous TiNiSn.

The measured and calculated elastic modulus data for amorphous TiNiSn are presented in figure 4. For comparison, the elastic modulus of bulk (crystalline) TiNiSn of 172 GPa is also provided [14], together with the corresponding DFT value at 0 K reaching 220 GPa [54]. As amorphous solids are expected to exhibit lower elastic moduli than the crystalline counterparts [53], the crystalline data [14] are taken as the upper bound. Using the Debye-Grüneisen approximation [55], the DFT-derived elastic modulus for amorphous TiNiSn was obtained as a function of temperature and stress. The machine learning predictions correspond to room temperature (due to the use of such input), but there is no temperature dependence included in the models. This was, however, considered by DFT in the current study (see also table 1). At room temperature (300 K), the DFT value is 113 GPa (stress-free conditions), which deviates −15% from the NI value. As the generalised gradient approximation was used in the DFT calculations, underestimation of the experimental data as well as the magnitude of the obtained deviation are acceptable [56]. It is also conceivable that the grown thin film exhibits some stress due to a difference in the thermal expansion coefficient between the sample and the substrate as well as ion bombardment during synthesis. Namely, residual stresses in the range of several GPa are commonly observed in thin films, e.g. −1.5 GPa in CrN and −2.2 GPa in Ta [57]. Accordingly, in the DFT model, hydrostatic stress was also considered. At 300 K and assuming compressive hydrostatic stress (−2 GPa), the DFT value reaches 126 GPa, which deviates only by −5% from the NI result (132 ± 1 GPa). The machine learning models, ANN and GBR, predicted the values of 87 and 78 GPa, respectively, (see figure 4) using $x_1 = 6.53$ g cm^{-3} (the DFT value obtained in this work) and $x_2 = 75.090$ g mol^{-1} (from the periodic table of elements). Although their performance is inferior to that of DFT, these models account for a wide range of possible amorphous solids and thus capture general trends. In cases where experimental data are unavailable, such models can provide rapid estimates, whereas DFT calculations are computationally intensive for amorphous systems.

It is expected that the elastic modulus is decreased as a function of temperature due to thermal expansion and hence effectively longer bonds [58], which can also be shown analytically [59–61]. However, the weak influence of temperature on the elastic properties of amorphous TiNiSn obtained in this work by DFT (see table 1) should further be discussed. If there are no short-range bond changes as a function of temperature, being equivalent to a lack of phase transitions in a crystalline system, the elastic modulus does not vary substantially, which was demonstrated for amorphous SiO_2 [62]. In the

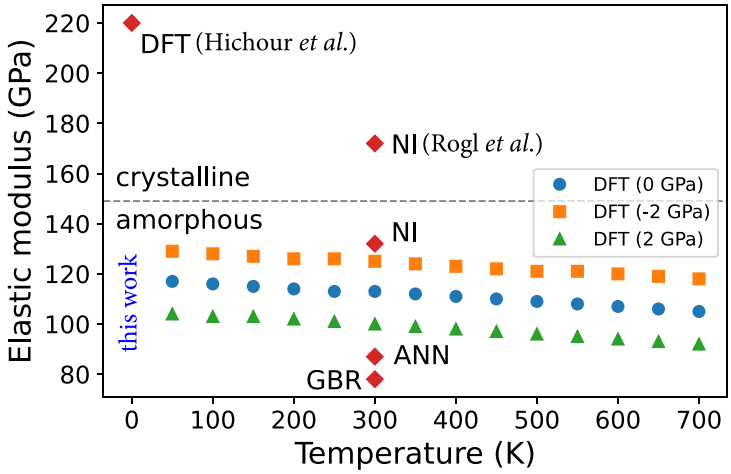

Figure 4. Elastic modulus of amorphous TiNiSn obtained by nanoindentation (NI), DFT and machine learning (ANN and GBR). DFT refers to the elasticity data without stress, unless stated otherwise. A comparison is made with crystalline (bulk) data from the literature: Rogl *et al* (experiment, NI on bulk samples) [14] and Hichour *et al* (DFT at 0 K) [54]. The error bars for the experimental data (NI) are not included since they would be covered by the symbols.

Table 1. Elastic modulus (in GPa) of amorphous TiNiSn obtained by DFT as a function of temperature and hydrostatic stress (compressive or tensile, 2 GPa).

Temperature (K)	Compressive stress	Stress-free	Tensile stress
50	129	117	104
100	128	116	103
150	127	115	103
200	126	114	102
250	126	113	101
300	125	113	100
350	124	112	99
400	123	111	98
450	122	110	97
500	121	109	96
550	121	108	95
600	120	107	94
650	119	106	93
700	118	105	92

current work, the upper temperature range was thus limited to 700 K. Furthermore, the machine learning models derived in this work do not capture temperature effects limiting their applicability to room temperature. There are many applications where this is sufficient, such as amorphous thin film transistors, various sensors, amorphous oxides for non-volatile memory, actuators operating at ambient conditions, amorphous solar cells, amorphous glass for integrated photonic circuits, packaging and amorphous electrodes in Li-ion batteries, to name a few.

It remains to rationalise the obtained elasticity data based on the electronic structure analysis, as shown in figure 5. Several observations can be made based on the electron density distribution. It is evident that the system is disordered. Ti, Ni and Sn share charge, which can be interpreted as a covalent contribution to the overall bonding. The electron density does not reach the minimum value, which points towards a metallic contribution to the bonding in amorphous TiNiSn. Smaller differences in electronegativity are present, but the ionic contribution is likely small. Hence, the covalent interaction between disordered Ti, Ni and Sn with some metallic contributions leads to strong bonds, which is consistent with the elastic modulus data in figure 4. It should also be noted that the bonding in amorphous TiNiSn is consistent with crystalline TiNiSn [63], but due to disorder (lower coordination) the elastic modulus is lower. This system is of relevance for applications in flexible and wearable devices. Having a correlation between its elasticity and electronic structure, future modulations in mechanical flexibility may be achieved. Amorphous TiNiSn exhibits promising transport properties, including a Seebeck coefficient of -2 μV K^{-1} [20] (which could be enhanced through doping), good electrical conductivity [20], and potentially very low thermal conductivity inferred from amorphous ZrNiSn data [23]. Combined

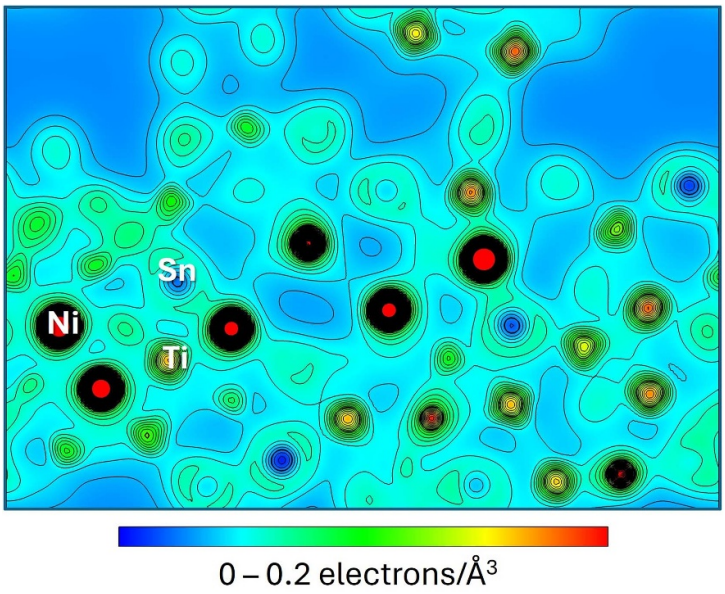

Figure 5. Electron density distribution in TiNiSn. A (110) cut through the amorphous configuration is shown.

with its mechanical robustness demonstrated in bending tests [21] and strong adhesion to organic substrates such as polymers, paper and textiles [21], this system shows significant potential for applications in flexible and wearable devices.

4. Conclusions

This study combines experimental measurements and theoretical modelling to elucidate the elastic behaviour of amorphous TiNiSn. NI of sputtered thin films revealed a high elastic modulus of 132 GPa, demonstrating that mechanical rigidity can be retained even in the absence of long-range order. Complementary DFT calculations yielded an elastic modulus of 113 GPa, and accounting for hydrostatic stress effects during film growth further reconciled theory with experiment. Analysis of the electronic structure shows that a network of predominantly covalent bonds, with minor metallic contributions, rationalises the system's stiffness. Machine learning models (ANN and GBR), while underestimating the elastic modulus value, capture relevant trends and provide a framework for broader screening of amorphous systems. These findings establish a coherent understanding of the elastic response of amorphous TiNiSn and highlight its promise as a mechanically robust component for flexible and wearable technologies. Non-equilibrium growth techniques, such as magnetron sputtering, employed at room temperature broaden the spectrum of possible substrates, such as polymers and textiles, opening avenues for further applications.

Data availability statement

All data that support the findings of this study are included within the article (and any supplementary files).

Supplementary data available at https://doi.org/10.1088/1361-648X/ae3c75/data1.

Acknowledgment

This work was financially supported by the Olle Engkvist Foundation (project number 217-0023). The computations were enabled by resources provided by the National Academic Infrastructure for Supercomputing in Sweden (NAISS) at National Supercomputer Centre (NSC) in Linköping partially funded by the Swedish Research Council through grant agreement no. 2022-06725.

Author contributions

Denis Music 0000-0003-2303-3676
Conceptualization (lead), Data curation (lead), Formal analysis (lead), Funding acquisition (lead), Investigation (lead), Methodology (equal), Project administration (lead), Resources (lead), Software (equal), Validation (equal), Visualization (lead), Writing – original draft (lead)

Balint I Hajas
Formal analysis (supporting), Investigation (supporting), Writing – review & editing (equal)

Paul H Mayrhofer
Formal analysis (supporting), Writing – review & editing (equal)

Sana Khayyamifar 0000-0001-7576-0387
Formal analysis (supporting), Investigation (supporting), Writing – review & editing (equal)

Grzegorz Sadowski 0000-0002-2857-5135
Formal analysis (supporting), Writing – review & editing (equal)

Johan Hektor 0000-0003-3454-2660
Formal analysis (supporting), Writing – review & editing (equal)

Pär A T Olsson 0000-0002-7606-1673
Formal analysis (supporting), Methodology (supporting), Writing – review & editing (equal)

References

[1] Everhart W and Newkirk J 2019 *Heliyon* **5** e01578
[2] Graf T, Felser C and Parkin S S P 2011 *Prog. Solid State Chem.* **39** 1
[3] Hinterleitner B *et al* 2019 *Nature* **576** 85
[4] Heusler F 1903 *Verh. Dtsch. Phys. Ges.* **12** 219
[5] Devarajan U, Singh S, Muthu E, Selvan G K, Sivaprakash P, Barman S R and Arumugam S 2014 *Appl. Phys. Lett.* **105** 252401
[6] Devarajan U, Sivaprakash P, Garg A B, Kim I and Arumugam S 2023 *J. Supercond. Nov. Magn.* **36** 1611
[7] Sivaprakash P, Muthu S E, Saravanan C, Rao N V R and Kim I 2023 *J. Appl. Phys.* **56** 495002
[8] Bos J-W G and Downie R A 2014 *J. Phys.: Condens. Matter* **26** 433201
[9] Felser C, Wollmann L, Chadov S, Fecher G H and Parkin S S P 2015 *APL Mater.* **3** 041518
[10] Elphick K, Frost W, Samiepour M, Kubota T, Takanashi K, Sukegawa H, Mitani S and Hirohata A 2021 *Sci. Technol. Adv. Mater.* **22** 235
[11] Dey P and Dutta B 2021 *Phys. Rev. Mater.* **5** 035407
[12] Liu Y, Fu C, Xia K, Yu J, Zhao X, Pan H, Felser C and Zhu T 2018 *Adv. Mater.* **30** 1800881
[13] Populoh S, Aguirre M H, Brunko O C, Galazka K, Lu Y and Weidenkaff A 2012 *Scr. Mater.* **66** 1073
[14] Rogl G *et al* 2016 *Acta Mater.* **107** 178
[15] Guo Z, Liu Z and Tang R 2024 *Mater. Chem. Front.* **8** 1703
[16] Biswas P, Tafen D N, Inam F, Cai B and Drabold D A 2009 *J. Phys.: Condens. Matter* **21** 084207
[17] Zhou Y, Tan Q, Zhu J, Li S, Liu C, Lei Y and Li L 2015 *J. Electron. Mater.* **44** 1957
[18] Kudryavtsev Y V, Melnik A K, Gościańska I, Dubowik J and Kravets A F 2021 *Eur. Phys. J. B* **94** 92
[19] Kudryavtsev Y V, Oksenenko V A, Lee Y P, Hyun Y H, Kim J B, Park J S, Park S Y and Dubowik J 2007 *Phys. Rev. B* **76** 024430
[20] Barzola-Quiquia J, Osmic E, Bercoff P G, Venosta L and Häussler P 2023 *J. Non-Cryst. Solids* **600** 121969
[21] Khayyamifar S, Sadowski G, Hektor J and Music D 2024 *Thin Solid Films* **807** 140534
[22] Oliver W C and Pharr G M 1992 *J. Mater. Res.* **7** 1564
[23] Music D, Khayyamifar S and Hektor J 2023 *Comput. Mater. Sci.* **230** 112530
[24] Music D, Geyer R W and Schneider J M 2016 *Surf. Coat. Technol.* **286** 178
[25] Ahilan K, Bennett M C, Aronson M C, Anderson N E, Canfield P C, Munoz-Sandoval E, Gortenmulder T, Hendrikx R and Mydosh J A 2004 *Phys. Rev. B* **69** 245116
[26] Kresse G and Hafner J 1993 *Phys. Rev. B* **48** 13115
[27] Kresse G and Hafner J 1994 *Phys. Rev. B* **49** 14251
[28] Kresse G and Joubert D 1999 *Phys. Rev. B* **59** 1758
[29] Perdew J P, Burke K and Ernzerhof M 1996 *Phys. Rev. Lett.* **77** 3865
[30] Monkhorst H J and Pack J D 1976 *Phys. Rev. B* **13** 5188
[31] Music D, Takahashi T, Vitos L, Asker C, Abrikosov I A and Schneider J M 2007 *Appl. Phys. Lett.* **91** 191904
[32] Holec D, Friak M, Neugebauer J and Mayrhofer P H 2012 *Phys. Rev. B* **85** 064101
[33] Momma K and Izumi F 2008 *J. Appl. Cryst.* **41** 653
[34] Schnabel V, Köhler M, Music D, Bednarcik J, Clegg W J, Raabe D and Schneider J M 2017 *J. Phys.: Condens. Mater.* **29** 265502
[35] Hostert C, Music D, Bednarcik J, Keckes J, Kapaklis V, Hjörvarsson B and Schneider J M 2011 *J. Phys.: Condens. Mater.* **23** 475401
[36] Stoica M, Das J, Bednarcik J, Franz H, Mattern N, Wang W H and Eckert J 2008 *J. Appl. Phys.* **104** 013522
[37] Zhang B, Zhao D Q, Pan M X, Wang R J and Wang W H 2006 *Acta Mater.* **54** 3025
[38] Guo Q, Zhang L, Zeiger A S, Li Y, Vliet K J V and Thompson C V 2011 *Scr. Mater.* **64** 41
[39] Minouei H, Akbari G H, Enayati M H and Hong S I 2017 *Mater. Sci. Eng. A* **682** 396
[40] Hu Y-J *et al* 2020 *npj Comput. Mater.* **6** 25

[41] Jambur V, Molina-Ruiz M, Dauer T, Horton-Bailey D, Vallery R, Gidley D, Metcalf T H, Liu X, Hellman F and Szlufarska I 2022 *J. Non-Cryst. Solids* **587** 121588
[42] Jantschner O, Field S K, Music D, Terziyska V L, Schneider J M, Munnik F, Zorn K and Mitterer C 2014 *Tribol. Int.* **77** 15
[43] Music D and Schneider J M 2008 *J. Phys.: Condens. Matter* **20** 195203
[44] Hunold O, Keuter P, Bliem P, Music D, Wittmers F, Ravensburg A L, Primetzhofer D and Schneider J M 2017 *J. Phys.: Condens. Matter* **29** 085404
[45] Music D, Hensling F, Pazur T, Bednarcik J, Hans M, Schnabel V, Hostert C and Schneider J M 2013 *Solid State Commun.* **169** 6
[46] Schneider J M, Larsson K, Lu J, Olsson E and Hjövarsson B 2002 *Appl. Phys. Lett.* **80** 1144
[47] Nayak G K, Srinivasan P, Todt J, Daniel R, Nicolini P and Holec D 2025 *Comput. Mater. Sci.* **249** 113629
[48] Music D, Xiao X, Naser R, Chang K, Sadowski G and Olsson P A T 2025 *Adv. Sci.* **12** e04627
[49] Schmidgall S, Ziaei R, Achterberg J, Kirsch L, Hajiseyedrazi P and Eshraghian J 2024 *APL Mach. Learn.* **2** 021501
[50] Bentéjac C, Csörgő A and Martínez-Muñoz G 2021 *Artif. Intell. Rev.* **54** 1937
[51] Yamada H, Liu C, Wu S, Koyama Y, Ju S, Shiomi J, Morikawa J and Yoshida R 2019 *ACS Cent. Sci.* **5** 1717
[52] Galimzyanov B N, Doronina M A and Mokshin A V 2023 *Physica A* **617** 128678
[53] Kurapov D, Reiss J, Trinh D H, Hultman L and Schneider J M 2007 *J. Vac. Sci. Technol. A* **25** 831
[54] Hichour M, Rached D, Khenata R, Rabah M, Merabet M, Reshak A H, Omran S B and Ahmedf R 2012 *J. Phys. Chem. Solids* **73** 975
[55] Söderlind P, Nordström L, Yongming L and Johansson B 1990 *Phys. Rev. B* **42** 4544
[56] Paier J, Marsman M, Hummer K, Kresse G, Gerber I C and Ángyán J G 2006 *J. Chem. Phys.* **124** 154709
[57] Abadias G, Chason E, Keckes J, Sebastiani M, Thompson G B, Barthel E, Doll G L, Murray C E, Stoessel C H and Martinu L 2018 *J. Vac. Sci. Technol. A* **36** 020801
[58] Hirata Y and Shimonosono T 2022 *J. Ceram. Soc. Japan.* **130** 264
[59] Varshni Y P 1970 *Phys. Rev. B* **2** 3952
[60] Olsson P A T 2023 *Comput. Mater. Sci.* **218** 111953
[61] Keuter P, Music D, Schnabel V, Stuer M and Schneider J M 2019 *J. Phys.: Condens. Matter* **31** 225402
[62] Bin L, Jing-Yang W, Yan-Chun Z and Fang-Zhi L 2008 *Chin. Phys. Lett.* **25** 2747
[63] Choudhary M K and Ravindran P 2019 *Sustain. Energy Fuels* **4** 895